

# Multilateral surface analysis of the CeB<sub>6</sub> electron-gun cathode used at SACLA XFEL

Takuo Ohkochi,<sup>a,b\*</sup> Takayuki Muro,<sup>a</sup> Eiji Ikenaga,<sup>a,‡</sup> Kazuaki Togawa,<sup>b</sup> Akira Yasui,<sup>a</sup> Masato Kotsugi,<sup>a,§</sup> Masaki Oura<sup>b</sup> and Hitoshi Tanaka<sup>b</sup>

<sup>a</sup>Japan Synchrotron Radiation Research Institute, Kouto, Sayo, Hyogo 679-5198, Japan, and <sup>b</sup>RIKEN SPring-8 Center, Kouto, Sayo, Hyogo 679-5148, Japan. \*Correspondence e-mail: o-taku@spring8.or.jp

Received 24 June 2021

Accepted 16 September 2021

Edited by K. Kvashnina, ESRF – The European Synchrotron, France

‡ Present address: Institute of Materials and Systems for Sustainability, Nagoya University, Furo-cho, Chikusa-ku, Nagoya 464-8603, Japan.

§ Present address: Faculty of Industrial Science and Technology, Tokyo University of Science, Katsushika, Tokyo 125-8585, Japan.

**Keywords:** thermally activated processes; photoemission; synchrotron radiation; microstructures; CeB<sub>6</sub>; LEEM; PEEM; TEEM; thermionic electron cathode.

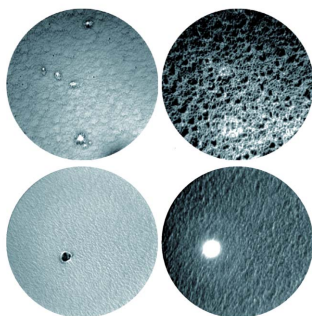
**Supporting information:** this article has supporting information at journals.iucr.org/s

The CeB<sub>6</sub>(001) single crystal used as a cathode in a low-emittance electron gun and operated at the free-electron laser facility SACLA was investigated using cathode lens electron microscopy combined with X-ray spectroscopy at SPring-8 synchrotron radiation facility. Multilateral analysis using thermionic emission electron microscopy, low-energy electron microscopy, ultraviolet and X-ray photoemission electron microscopy and hard X-ray photoemission spectroscopy revealed that the thermionic electrons are emitted strongly and evenly from the CeB<sub>6</sub> surface after pre-activation treatment (annealing at 1500°C for >1 h) and that the thermionic emission intensity as well as elemental composition vary between the central area and the edge of the old CeB<sub>6</sub> surface.

## 1. Introduction

SACLA (SPring-8 Angstrom Compact free-electron LAsER), the X-ray free-electron laser (XFEL) facility in Japan (Ishikawa *et al.*, 2012), boasts a compact body which is attained by an in-vacuum undulator system and extremely stable laser pulse emission. Instead of using a photocathode, which is popular at XFEL facilities worldwide, a thermionic electron cathode is used to provide low-emittance electron beams of high stability over a long duration. The CeB<sub>6</sub>(001) single-crystal cathode with ~3 mm diameter is activated by heating to ~1500°C and an initial electron beam with a beam energy of 500 keV, peak current of 1 A, pulse width of 3 µs, repetition rate of 60 Hz and normalized emittance of ~0.6 mm mrad (r.m.s.) have been provided routinely (Togawa *et al.*, 2007). Nevertheless, the degradation of the emission power over a very long term operation is still unavoidable; initially, the cathode can emit over ~1 A at only 1450°C, then it gradually requires increasing of the temperature to maintain its emission level, and finally is unable to emit 1 A even if it is heated thoroughly to 1550–1600°C. The cathodes have been changed about once a year, so determining the cause of cathode degradation is critical for more reliable beam activity.

Meanwhile, a cathode lens microscope, specifically the spectroscopic photoemission and low-energy electron microscope (SPELEEM) combined with synchrotron radiation (SR) X-rays, is a powerful instrument for studying the physical and chemical properties of the thermionic cathode materials at both microscopic and macroscopic levels. Low-energy electron microscopy (LEEM) (Teliëps & Bauer, 1985; Bauer, 2019), photoemission electron microscopy (PEEM) and other forms of electron emission microscopy are among the observation modes available in SPELEEM. In the LEEM mode, an incident electron beam with minus few tens of kV of acceleration voltage ( $E_{HV}$ ) is decelerated at a sample biased at  $E_{HV} + E_{STV}$



(in which a start voltage  $E_{STV}$  is typically 0–50 V), *i.e.* the effective incident electron energy ( $E_{STV}$ ) is low and thus the generated electron image represents well the surface electronic states of the sample. Different kinds of electrons like the reflected, inelastically scattered, Auger and secondary electrons can be visualized selectively by choosing appropriate  $E_{STV}$ . By changing the lens parameters to reciprocal-space imaging mode, low-energy electron diffraction patterns can be obtained. However, lights rather than electron beams are used as photoemission excitation sources in the PEEM mode. Ultraviolet (UV) lights are used to obtain the spatial distribution of surface work functions of materials, while synchrotron radiation X-rays help to visualize information equivalent to X-ray absorption spectroscopy (XAS), X-ray magnetic circular/linear dichroism (XMCD/XMLD), X-ray photoemission spectroscopy, and so on. Besides the functions of LEEM and PEEM as explained above, the SPELEEM can project other types of electrons emitted from the specimen. For instance, field emission electrons emitted from irregular or sharpened material surfaces by applying a strong electric field are regarded as an undesirable background for LEEM/PEEM observations, while thermionic emission electrons, derived from materials with low work functions under high temperature, can be a good object for microscopic investigations of thermionic cathode materials. Though the possibility of thermionic emission-electron microscopy (TEEM) has been mentioned since the beginning of the instrumental development of cathode lens microscopy (Bauer, 1994), there have been few reports on TEEM observations (Fukidome *et al.*, 2006; Lu *et al.*, 2018, 2020).

In this study, we report on surface-state investigations of CeB<sub>6</sub>(001) single-crystal ingots used as an electron-gun cathode at SACLA. TEEM observations of a pristine CeB<sub>6</sub> sample (having the same shape as the CeB<sub>6</sub> used in SACLA) revealed that the initial 1500°C annealing was necessary to remove a surface-oxidized layer and to exert a good emission power evenly over the entire surface. We also discovered that thermionic emissions were more significant at the step edges rather than at the flat terraces in the purified (annealed) surface. Control experiments between pristine and used (employed in SACLA for ~1 year) CeB<sub>6</sub> by TEEM, LEEM, UV and X-ray PEEM (UV-PEEM and X-PEEM) and hard X-ray photoemission spectroscopy (HAXPES) revealed that the long period operation causes inhomogeneity in the elemental composition, and the thermionic electron emission power on the CeB<sub>6</sub> surface between the center and the edge and possible origins are discussed.

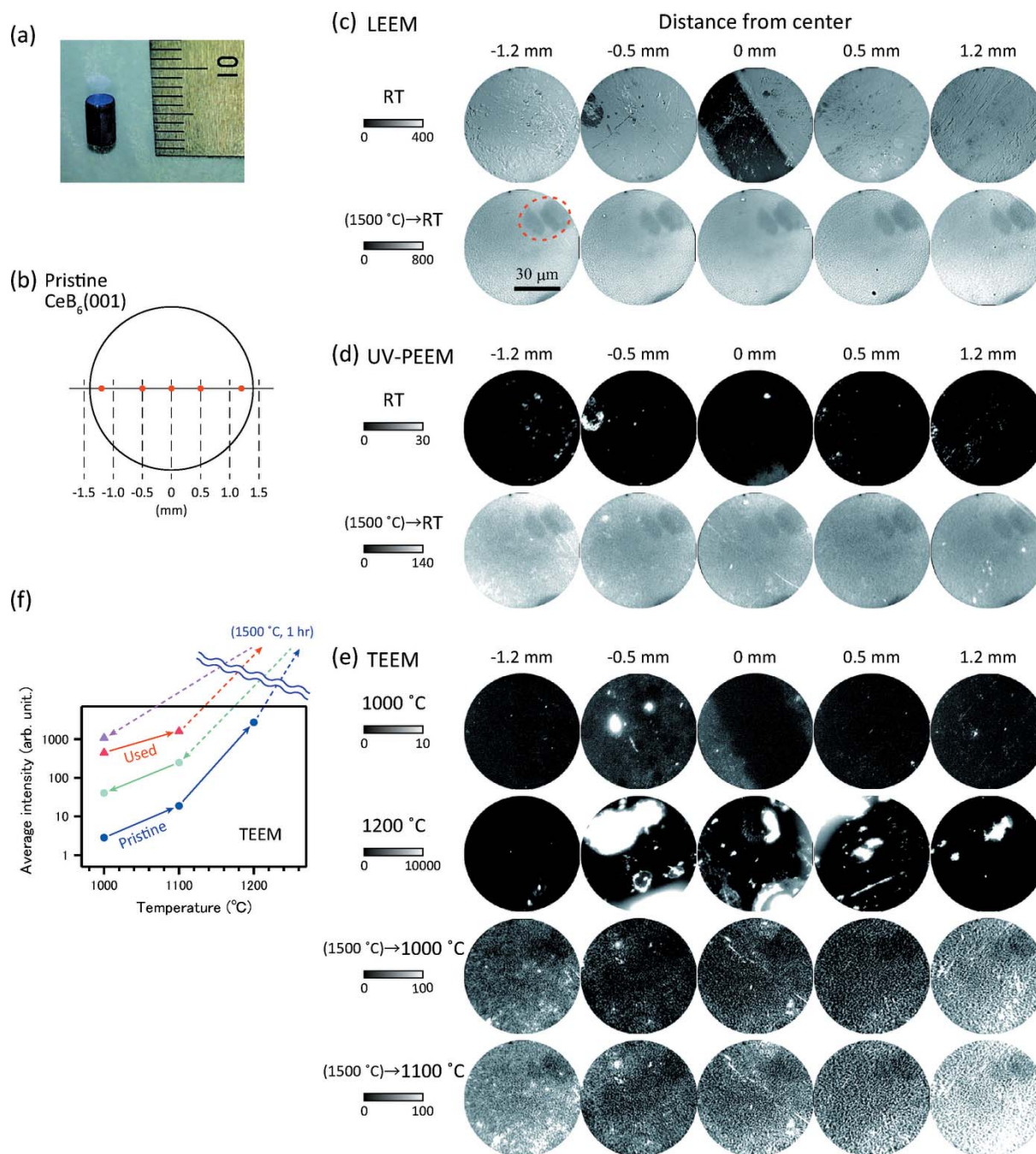
## 2. Experimental

The samples used in this study were commercial CeB<sub>6</sub>(001) single-crystal ingots (APTech Inc., USA) of ~3 mm diameter and 5 mm length with mirror-polished surfaces [Fig. 1(a)]. Microscopic measurements were performed using a SPELEEM apparatus [LEEM III with imaging energy analyzer (ELMITEC GmbH)] (Guo *et al.*, 2007) incorporated at the BL17SU soft X-ray beamline at SPring-8 (Ohashi *et al.*,

2007; Senba *et al.*, 2007) with which LEEM, UV-PEEM, X-PEEM (and XAS) and TEEM observations are available in the same field-of-view (FOV). Photon and electron sources used in these observations were: LEEM – electron beam (LaB<sub>6</sub>, –20 kV); UV-PEEM – high-pressure mercury lamp; and X-PEEM – soft X-rays produced from a multi-polarization-mode undulator (Shirasawa *et al.*, 2004). Meanwhile, without using any external sources, TEEM images were obtained by simply heating the sample to 1000–1200°C. The sample was mounted on an ELMITEC standard sample holder, which can withstand temperatures up to ~1200°C (~2000°C for short flashing). For macroscopic chemical analysis, we used a HAXPES apparatus (Woicik, 2016; Ikenaga *et al.*, 2013) installed at the BL47XU hard X-ray beamline and systematically investigated the composition variation in the CeB<sub>6</sub> from the point of view of the position-dependence of core-electron peaks' intensities of the constituent elements. A size of the beam footprint on the sample for the HAXPES measurement was 0.04 mm (w) × 1 mm (h), where w and h correspond to the directions that are parallel and perpendicular to the scanning direction, respectively. Approximate probing depths are less than 1 nm for LEEM, several nanometres for PEEM and TEEM, and several tens of nanometres for HAXPES.

## 3. Results and discussion

Figs. 1(c), 1(d) and 1(e), respectively, show LEEM, UV-PEEM and TEEM images (diameter of FOV: 75 μm) of a pristine CeB<sub>6</sub>(001) single crystal at the representative positions shown in Fig. 1(b) (note that the grayscale of the images is different for each condition). Due to mechanical and thermal drift, at the same (nominal) distance from the center, slight differences in the measurement position between different measurement conditions are noted [the same is true for Figs. 3 and Fig. 4(b) shown later]. Two dark stain-like patterns (exemplified by a red dotted circle) are unwanted burned areas of the micro-channel plate (MCP) caused by thermionic emission electron's overexposure. The LEEM and PEEM images are taken at room temperature (RT) before and after annealing at 1500°C for about an hour (*in situ* at the main experimental chamber). The LEEM images shown in Fig. 1(c) are obtained with  $E_{STV}$  set to ~0 V, which corresponds to surface topology observations [so-called mirror electron microscopy (MEM)]. The annealing process flattens out the rough surface with some scratches (*e.g.* a large ditch-like structure found at 0 mm). A similar tendency can be found from the UV-PEEM images in Fig. 1(d). Furthermore, annealing significantly improved the overall PEEM image intensity, presumably due to the reduction of the oxidized surface (note that the number of photoemission electrons at the UV range well reflects the surface work function). The temperature dependence of the TEEM image intensities [Fig. 1(e)] also follows the trend of the UV-PEEM results, that is, the thermionic emission is sporadic for all observed temperatures (1000 and 1200°C) before the 1500°C annealing but it becomes homogeneous after annealing. Although the TEEM observations were planned to


**Figure 1**

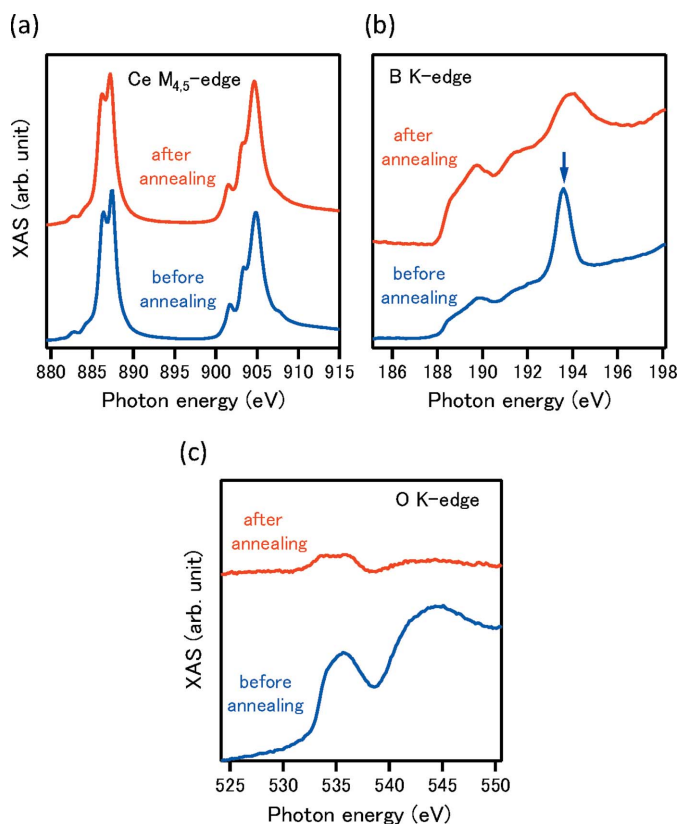
(a) Photograph of the  $\text{CeB}_6(001)$  single crystal. (b) Drawing of a pristine  $\text{CeB}_6$  surface in which areas for LEEM/PEEM/TEEM observations are indicated by red dots. (c) LEEM, (d) UV-PEEM and (e) TEEM images of pristine  $\text{CeB}_6$  at representative areas with different temperature. The diameter of the field of view is  $75\ \mu\text{m}$  for all the images. The grayscale of the images (shown by scale bars) are varied for different conditions in order to show the image contrast clearly. (f) Temperature dependence of the average TEEM image intensities. Note that the intensities at  $1500^\circ\text{C}$  were much higher than the detection limit and were not measured (dashed arrows are shown to indicate histories of annealing).

be performed at temperatures up to  $\sim 1500^\circ\text{C}$ , *i.e.* similar temperature as the SACLA operation, the electron emission at that temperature reaches as high as  $\sim 1\ \text{A}$ , which far exceeds the interlock limit of the SPELEEM's objective lens ( $\sim 130\ \text{mA}$ ). Therefore, we decided to obtain images within  $1000$ – $1200^\circ\text{C}$ , although the annealing treatment up to  $\sim 1500^\circ\text{C}$  was performed *in situ* in the main observation chamber with  $E_{\text{HV}}$  turned off. We confirmed that the TEEM

contrast after annealing [third and fourth rows of Fig. 1(e)] is analogous between  $1000^\circ\text{C}$  and  $1100^\circ\text{C}$  for all the positions and hence the suppressed observation temperature may not affect qualitative discussion. The temperature-dependence of the TEEM image intensity averaged over all the observed areas is shown in Fig. 1(f) [blue markers and arrows for pristine  $\text{CeB}_6$ ; details of the results for used  $\text{CeB}_6$  (red markers and arrows) are explained later]. The unit of intensity values is

arbitrary but unified for all LEEM/PEEM/TEEM observations in this article, by calibrating with the amplification rates determined by MCP voltages. At the initial heating process, dramatic increases of the thermionic emission by approximately one and two orders of magnitude for  $1000^{\circ}\text{C} \rightarrow 1100^{\circ}\text{C}$  and  $1100^{\circ}\text{C} \rightarrow 1200^{\circ}\text{C}$ , respectively, are observed. As for the effect of  $1500^{\circ}\text{C}$  annealing, the thermionic emission is improved by approximately one order of magnitude after annealing, according to the comparison at the same temperature (e.g. 2.8 and 40 at  $1000^{\circ}\text{C}$  before and after annealing, respectively).

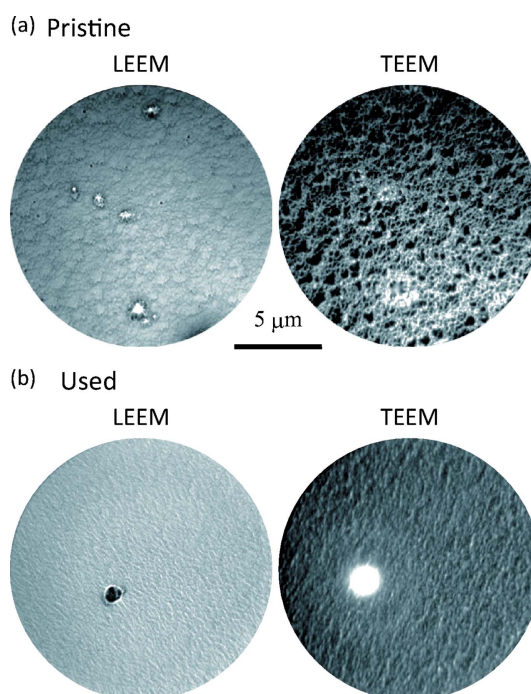
XAS spectra of pristine  $\text{CeB}_6$  at the  $\text{Ce } M_{4,5}$ -, B  $K$ - and O  $K$ -absorption edges were drawn by extracting X-PEEM image intensities with sweeping photon energies across the absorption edges, as shown in Fig. 2 (representative X-PEEM images for Ce  $M_{4,5}$ - and B  $K$ -edges are shown later in Fig. 8). The temperature for X-PEEM observations ( $\sim 600^{\circ}\text{C}$ ) is low enough to remove the thermionic electron emission but high enough to prevent synchrotron radiation irradiation from contaminating the sample. The spectral shape after annealing (red line) in the Ce  $M_{5}$ -edge region [Fig. 2(a)] shows a double-peak structure, which is typical for the  $\text{Ce}^{3+}$  state (Mitra *et al.*, 2003) and is similar to the previously reported spectral shape of  $\text{CeB}_6$  (Magnuson *et al.*, 2001). The surface chemical state seems to remain unchanged since the overall shape of the Ce  $M_{4,5}$ -edge spectrum does not change by the annealing.



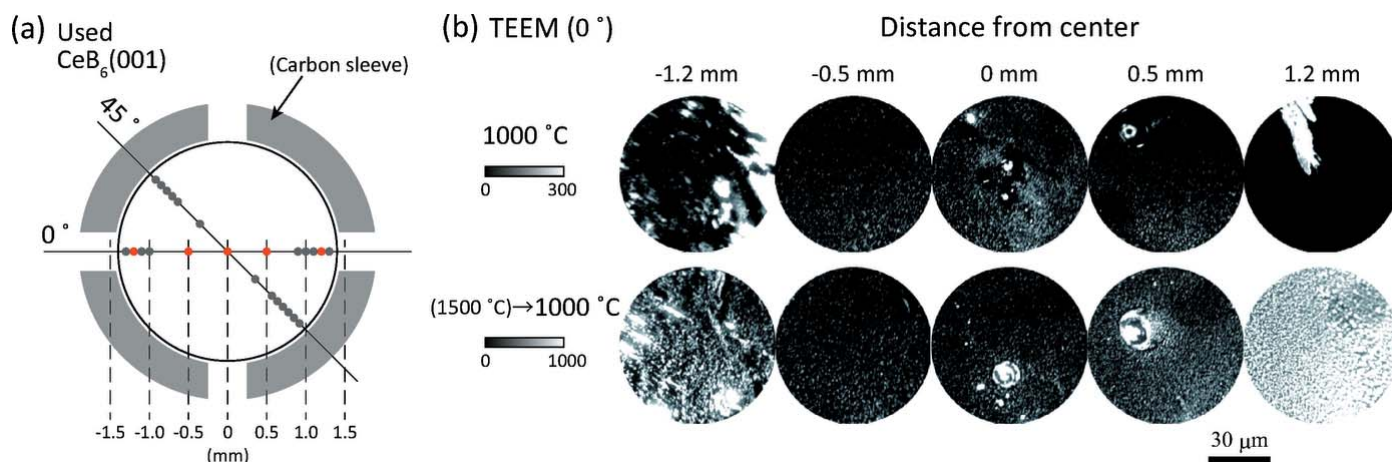
**Figure 2** XAS spectra ( $600^{\circ}\text{C}$ ) of pristine  $\text{CeB}_6$  before (blue line) and after (red line)  $1500^{\circ}\text{C}$  annealing obtained at the (a) Ce  $M_{4,5}$ -edge, (b) B  $K$ -edge and (c) O  $K$ -edge. All the spectra are normalized to the intensities at the pre-edge regions and displayed with vertical offset.

However, it does not rule out the possibility that cerium oxide existed before annealing because the cerium is trivalent also in  $\text{Ce}_2\text{O}_3$ . In fact, the spectral change in the B  $K$ -edge region is striking, as shown in Fig. 2(b). The sharp peak observed at  $193.6\text{ eV}$  before annealing (blue arrow) was greatly suppressed after annealing. We consider that this peak originates from boron oxide because the reported B  $K$ -edge XAS spectrum of  $\text{B}_2\text{O}_3$  showed a similar sharp peak around  $194\text{ eV}$  (Gilbert *et al.*, 2000). We also verified substantial suppression of the absorption structure around the O  $K$ -edge [Fig. 2(c)]. From these results, we conclude that the enhancement of the electron emission observed in the UV-PEEM and TEEM results in Figs. 1(d) and 1(e) is associated with the reduction of the surface oxide.

Fig. 3(a) shows magnified LEEM ( $600^{\circ}\text{C}$ ) and TEEM ( $1000^{\circ}\text{C}$ ) images (diameter of FOV:  $15\text{ }\mu\text{m}$ ) taken at the center of the pristine  $\text{CeB}_6$  after the annealing process. A fine but clear step-and-terrace structure is recognized from the LEEM image. Although the fine structure in the TEEM image is similar to that in the LEEM image, the intensity contrast is opposite; thermionic emission is more significant from the step edges than from the flat terraces. The result is convincing, considering the general fact that the field emission electrons are salient around sharpened edges. Note that no field emission electrons are recognized under the LEEM/PEEM observations at RT. Fig. 3(b) shows similar images as Fig. 3(a) taken for a  $\text{CeB}_6(001)$  ingot, which had operated as the electron-gun cathode at SACLA for about a year (we refer to this sample as ‘used  $\text{CeB}_6$ ’ hereafter). This sample does not show a clear step-and-terrace pattern as found in the pristine one but



**Figure 3** (a) Magnified LEEM ( $600^{\circ}\text{C}$ ) and TEEM ( $1000^{\circ}\text{C}$ ) images of pristine  $\text{CeB}_6$  after  $1500^{\circ}\text{C}$  annealing. (b) Similar images as (a) of used  $\text{CeB}_6$  after  $1500^{\circ}\text{C}$  annealing.


**Figure 4**

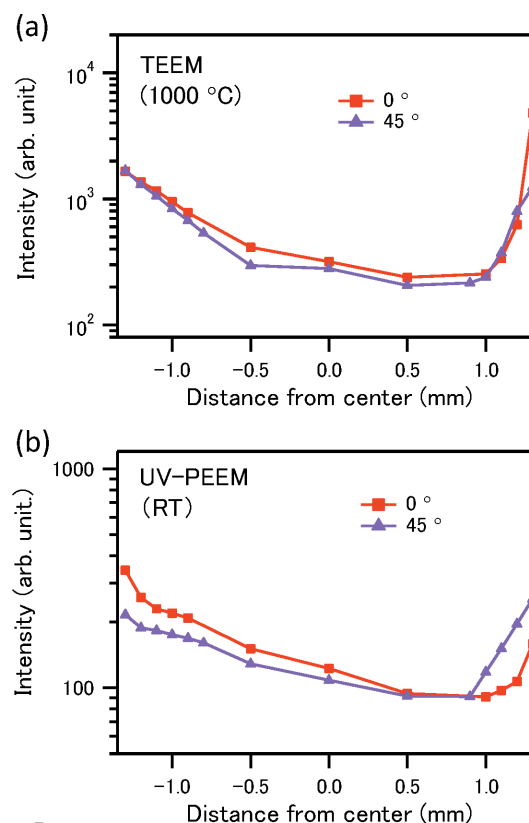
(a) Drawing of used  $\text{CeB}_6(001)$  surface with image acquisition positions [red dots: this figure (b); gray dots: Figs. SM1 ( $0^\circ$ ) and SM2 ( $45^\circ$ ) of the supporting information]. (b) TEEM images of used  $\text{CeB}_6$  at representative positions along the  $0^\circ$  direction taken at  $1000^\circ\text{C}$  before and after  $1500^\circ\text{C}$  annealing. Grayscale of the images (shown by scale bars) are varied for different conditions in order to show the image contrast clearly.

the surface roughness ( $<100\text{ nm}$ ) is still low enough to provide a low-emittance beam required at SACLA.

Fig. 4(b) shows position-dependent TEEM images of the used  $\text{CeB}_6(001)$  taken at  $1000^\circ\text{C}$  before and after the  $1500^\circ\text{C}$  annealing for  $\sim 1\text{ h}$  [image acquisition points are shown by red dots in Fig. 4(a)]. The full profile of the TEEM, LEEM and UV-PEEM images is shown in Figs. SM1 and SM2 of the supporting information [image acquisition points are indicated by red and gray dots in Fig. 4(a)]. The chemical and electron emission properties of  $\text{CeB}_6$  may be anisotropic, based on the shape and position of the sleeves of the graphite heater used to heat it during the SACLA process [see schematic drawing in Fig. 4(a)]. The probing direction which includes and excludes the points of contact with the carbon sleeves is ' $45^\circ$ ' and ' $0^\circ$ ', respectively. The surface of the used  $\text{CeB}_6$  [Fig. 4(b)] is slightly rougher than that of pristine  $\text{CeB}_6$  before annealing [Fig. 1(e)]. The roughness is mostly wiped out by annealing treatment, though some prominent defects remain. The temperature dependence of the average TEEM intensity of the used  $\text{CeB}_6$  is shown in Fig. 1(f) with red markers and arrows. Although the thermionic emission is improved by annealing, the increment is not very dramatic as in the case of the pristine  $\text{CeB}_6$  (blue plots), suggesting that the oxidized layer formed by exposure to the air (existing before annealing) is not so thick for the used  $\text{CeB}_6$  surface as for the pristine surface, due to the long-period activation in SACLA. Meanwhile, the intensity at  $1000^\circ\text{C}$  after annealing is lower for pristine  $\text{CeB}_6$  (40.7) than for used  $\text{CeB}_6$  (1074), being incompatible with the fact that the emission power has deteriorated over a long-period operation. Although the reason for this result is unclear, we believe that the annealing condition in this experiment did not accurately represent the actual operation condition in SACLA, *i.e.* the annealing time of  $\sim 1\text{ h}$  at  $1500^\circ\text{C}$  was insufficient to thoroughly purify the virgin  $\text{CeB}_6$  surface and obtain maximum emission power (the actual cathode is continuously heated about  $1500^\circ\text{C}$  during SACLA operation). In fact, the absorption fine structure at the oxygen  $K$ -edge is not completely eliminated by the  $\sim 1\text{ h}$  annealing [Fig. 2(c)]. Note

that since the limit of continuous heating of the SPELEEM manipulator is supposed to be up to  $\sim 1200^\circ\text{C}$ , we must give up further annealing for fear of damaging the insulating ceramics in the manipulator.

The sample position and scanning azimuth dependence of TEEM ( $1000^\circ\text{C}$ ) and UV-PEEM (RT) image intensity of used  $\text{CeB}_6$  after annealing is summarized in Fig. 5. The TEEM image intensity [Fig. 5(a)] is significantly higher around the


**Figure 5**

Line profiles of (a) TEEM ( $1000^\circ\text{C}$ ) and (b) UV-PEEM (RT) image intensities of used  $\text{CeB}_6$  after  $1500^\circ\text{C}$  annealing along the  $0^\circ$  and  $45^\circ$  directions.

edges than around the center. Although this tendency may partly be attributed to extrinsic factors such as an inhomogeneous temperature within the ingot surface, we assume that it is mainly derived from the variation of surface work functions, since the profile of UV-PEEM intensities [Fig. 5(b)] measured at RT show a similar tendency.

For comparison, Fig. 6 shows an example of a HAXPES spectrum [ $h\nu = 7.94$  keV, center of ingot, Fig. 6(a)] and position-dependence ( $0^\circ$  direction) of the Ce 4*p*, B 1*s* and C 1*s* peak intensities [Fig. 6(b)] of used CeB<sub>6</sub> obtained at RT. Note that the annealing procedure was not performed due to the HAXPES experimental station's instrument limitation. The B 1*s* and Ce 4*p* peaks abruptly decrease around the edge of the ingot while the C 1*s* peak increases, suggesting that the surface is contaminated by the carbon sleeve or the boron atoms are partially replaced by the carbon atoms. However, thermionic electrons are rather enhanced around the edge of used CeB<sub>6</sub> [Fig. 5(a)]. Furthermore, the overall shapes of the intensity profiles are similar between C/Ce [inset of Fig. 6(b)], TEEM [Fig. 5(a)] and UV-PEEM [Fig. 5(b)], and the tendency of the TEEM intensity profile is not so different between the  $0^\circ$  and  $45^\circ$  directions. Therefore, it seems that the carbon impurity does not significantly contribute to the degradation of the electron emission power but rather contributes to the suppression of the degradation. Another possible factor of the

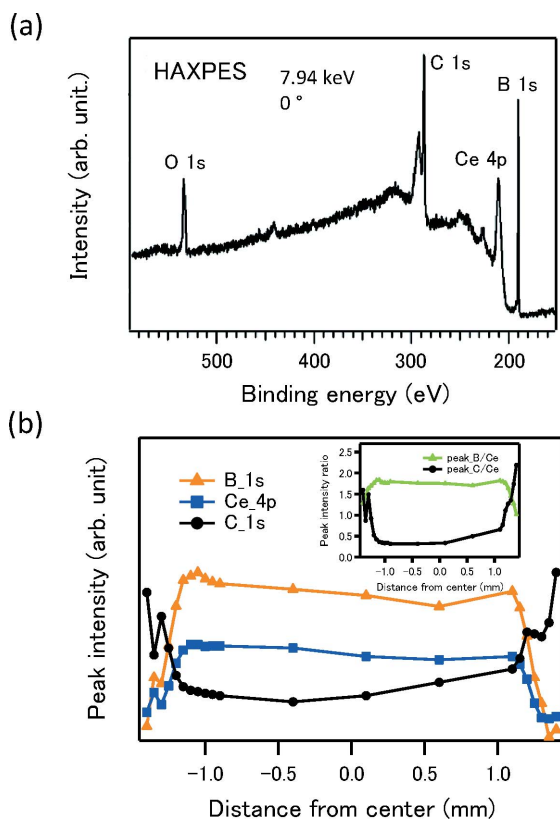


**Figure 6** (a) HAXPES spectra taken with a photon energy of 7.94 keV (distance from center: 0 mm) and (b) position-dependence (along  $0^\circ$  direction) of Ce 4*p*, B 1*s* and C 1*s* core photoemission peaks intensities of used CeB<sub>6</sub> taken at RT. The inset shows a similar plot but indicated as peak intensity ratio, B/Ce and C/Ce.

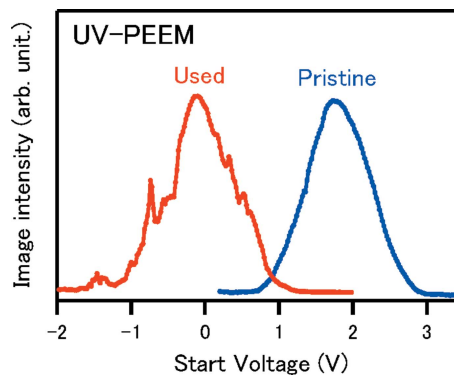


**Figure 7** Intensity profile of UV-PEEM images of pristine and used CeB<sub>6</sub> as a function of  $E_{STV}$  obtained at RT after annealing around the center of the ingot.

age-related deterioration is a compositional deviation from CeB<sub>6</sub> by long-period hard heating, which may occur on the entire surface. The chemical bond of the cerium atoms buried in the center of the B<sub>6</sub> network with firm covalent bond is relatively weak, causing the cerium atoms to be preferentially evaporated at the thermal-excitation state (Gurin *et al.*, 2001).

Fig. 7 shows the  $E_{STV}$  dependence of UV-PEEM image intensities for pristine and used CeB<sub>6</sub> samples obtained at RT after the annealing, as indirect evidence of compositional change (Ce evaporation) over the long SACLA operation [for images at representative  $E_{STV}$  (see Fig. SM3 of the supporting information)]. In PEEM observations,  $E_{STV}$  corresponds to the energy of secondary electrons that go through the energy slit at the exit of the electron analyzer (energy resolution  $\Delta E \simeq 1$  eV). In our LEEM apparatus, the intensity peak should be observed around  $E_{STV} = 1-2$  V, taking into account the work function of CeB<sub>6</sub> ( $\sim 2.6$  eV) (Lafferty, 1951). While the pristine CeB<sub>6</sub> (blue line) shows the expected result, the  $E_{STV}$  peak of the used CeB<sub>6</sub> (red line) shows an unusual value of  $\sim 0$  V. Additionally, the image intensity is unstable, as shown by the noisy or spiky intensity curve for the used CeB<sub>6</sub> (red line). These results suggest the charging of the surface of the used CeB<sub>6</sub>. Note that the  $E_{STV}$  dependence in Fig. 7 was not measured near the ingot edge, where the carbon contamination was prominent, but around the center of the CeB<sub>6</sub> surface. CeB<sub>6</sub> has good electric conductivity (the order of  $10 \mu\Omega$  cm) (Greiner & Gutowski, 1957), while pure boron is a semi-metal whose resistivity is of the order of 1–10 M $\Omega$  cm at RT (Tanaka *et al.*, 1980). Considering that the electric conductivity of boron-based materials is sensitive to their chemical states, the observed charging behavior supports the possibility that a more salient increase of the B 1*s* peak than its Ce 4*f* counterpart (*i.e.* larger B/Ce ratio) around the center of the cathode seen in Fig. 6(b) is caused by the compositional deviation from CeB<sub>6</sub>; cerium is poorly contained on the used CeB<sub>6</sub> surface.

Meanwhile, the X-PEEM result revealed no compositional inhomogeneity on a microscopic scale. Fig. 8 shows surface chemical contrast maps of the pristine and used CeB<sub>6</sub> samples obtained by taking the X-PEEM images around the Ce M<sub>5</sub>-

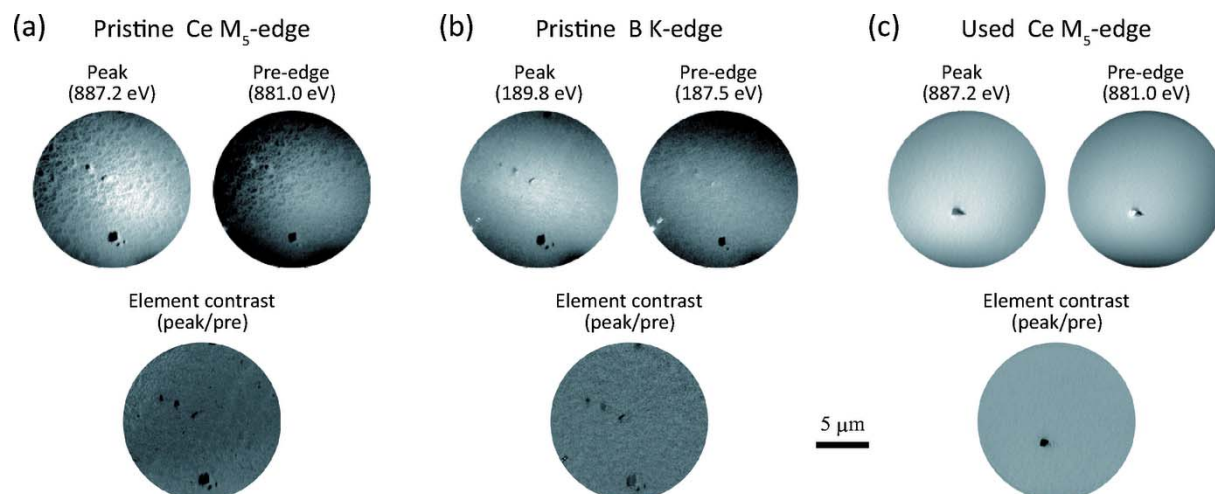


**Figure 8**

X-PEEM images taken at absorption-peak and pre-edge energies with their divided (element contrast) images. (a) Ce  $M_5$ -edge of pristine  $CeB_6$ , (b) B  $K$ -edge of pristine  $CeB_6$  and (c) Ce  $M_5$ -edge of used  $CeB_6$ .

and B  $K$ -edges (after annealing,  $\sim 600^\circ C$ ). The element contrast maps are obtained by dividing the image obtained at the peak top energy of the corresponding absorption edge by that obtained at the pre-edge region [examples of full XAS spectra around Ce  $M_5$ - and B  $K$ -edges are shown in Figs. 2(a) and 2(b), respectively]. The imaging areas are identical to those shown in Figs. 3(a) and 3(b) for pristine and used samples, respectively. Note that B  $K$ -edge images of used  $CeB_6$  were unavailable, since the low photon energy region ( $< 450$  eV) was inaccessible at that time due to an accident in the insertion device of BL17SU. The image contrast, seen both in the peak (887.2 eV) and pre-edge (881.0 eV) energies around the Ce  $M_5$ -edge of pristine  $CeB_6$  [Fig. 8(a)], which is analogous to that found in the TEEM image [Fig. 3(a)], disappeared in the element contrast image (peak/pre). This indicates that the contrast seen in the raw X-PEEM images (at peak and pre-edge) is not derived from chemical inhomogeneity but from any other factors such as topological unevenness, defects and contamination by other elements. The same tendency is also seen in the elemental contrast image around the B  $K$ -edge of pristine  $CeB_6$  [Fig. 8(b)] and around the Ce  $M_5$ -edge of used  $CeB_6$  [Fig. 8(c)], *i.e.* there is practically no chemical inhomogeneity when observed microscopically, even in the used  $CeB_6$ . Therefore, we conclude that, if the preferential evaporation of the cerium atoms was occurring during the thermionic emission, the Ce atoms were evaporated evenly.

#### 4. Conclusion

In conclusion, we implemented a multilateral surface analysis of  $CeB_6(001)$  single crystals used as the electron-gun cathode at SACLA XFEL, using TEEM, LEEM, UV-PEEM, X-PEEM and HAXPES. The TEEM observations revealed that homogeneous and strong electron emission power was exerted after annealing treatment up to  $\sim 1500^\circ C$  and that the annealed surface of the pristine  $CeB_6$  showed a step-and-

terrace structure in which the step edges emitted stronger thermionic electrons than flat terraces. Through further analysis including X-rays spectroscopy we found an increase in the electron emission as well as a variation in the elemental composition around the edge of the used  $CeB_6$  cathode. Even though the discussion based on the possible reasons, carbon influx and preferential evaporation of the cerium has not been conclusive, the findings in this study significantly push the project, *i.e.* development of the viable cathode, to the ultimate goal, as well as show the strength of the cathode lens microscopy combined with synchrotron radiation spectroscopy as a tool to investigate the surface of thermionic emission-electron materials.

#### Acknowledgements

The experiments at SPring-8 were performed with the approval of the Japan Synchrotron Radiation Research Institute (Proposal Nos. 2016A1317 (BL17SU) and 2016B1446 (BL47XU)) and RIKEN SPring-8 Center (Proposal Nos. 20190060 (BL17SU), 20200037 (BL17SU)). TO thanks Enago (<https://www.enago.jp>) for the English language review.

#### References

- Bauer, E. (1994). *Rep. Prog. Phys.* **57**, 895–938.
- Bauer, E. (2019). *Handbook of Microscopy*, edited by P. W. Hawkes & J. C. H. Spence, pp. 487–535. Springer.
- Fukidome, H., Yoshimura, M. & Ueda, K. (2006). *Jpn. J. Appl. Phys.* **45**, 70–72.
- Gilbert, B., Perfetti, L., Fauchoux, O., Redondo, J., Baudat, P., Andres, R., Neumann, M., Steen, S., Gabel, D., Mercanti, D., Ciotti, M. T., Perfetti, P., Margaritondo, G. & De Stasio, G. (2000). *Phys. Rev. E*, **62**, 1110–1118.
- Greiner, E. S. & Gutowski, J. A. (1957). *J. Appl. Phys.* **28**, 1364–1365.
- Guo, F. Z., Muro, T., Matsushita, T., Wakita, T., Ohashi, H., Senba, Y., Kinoshita, T., Kobayashi, K., Saitoh, Y., Koshikawa, T., Yasue, T., Oura, M., Takeuchi, T. & Shin, S. (2007). *Rev. Sci. Instrum.* **78**, 066107.

- Gurin, V. N., Korsukova, M. M., Loginov, M. V. & Shrednik, V. N. (2001). *Tech. Phys. Lett.* **27**, 431–433.
- Ohashi, H., Senba, Y., Kishimoto, H., Miura, T., Ishiguro, E., Takeuchi, T., Oura, M., Shirasawa, K., Tanaka, T., Takeuchi, M., Takeshita, K., Goto, S., Takahashi, S., Aoyagi, H., Sano, M., Furukawa, Y., Ohata, T., Matsushita, T., Ishizawa, Y., Taniguchi, S., Asano, Y., Harada, Y., Tokushima, T., Horiba, K., Kitamura, H., Ishikawa, T. & Shin, S. (2007). *AIP Conf. Proc.* **879**, 523–526.
- Ikenaga, E., Kobata, M., Matsuda, H., Sugiyama, T., Daimon, H. & Kobayashi, K. (2013). *J. Electron Spectrosc. Relat. Phenom.* **190**, 180–187.
- Ishikawa, T., Aoyagi, H., Asaka, T., Asano, Y., Azumi, N., Bizen, T., Ego, H., Fukami, K., Fukui, T., Furukawa, Y., Goto, S., Hanaki, H., Hara, T., Hasegawa, T., Hatsui, T., Higashiya, A., Hirono, T., Hosoda, N., Ishii, M., Inagaki, T., Inubushi, Y., Itoga, T., Joti, Y., Kago, M., Kameshima, T., Kimura, H., Kirihara, Y., Kiyomichi, A., Kobayashi, T., Kondo, C., Kudo, T., Maesaka, H., Maréchal, X. M., Masuda, T., Matsubara, S., Matsumoto, T., Matsushita, T., Matsui, S., Nagasono, M., Nariyama, N., Ohashi, H., Ohata, T., Ohshima, T., Ono, S., Otake, Y., Saji, C., Sakurai, T., Sato, T., Sawada, K., Seike, T., Shirasawa, K., Sugimoto, T., Suzuki, S., Takahashi, S., Takebe, H., Takeshita, K., Tamasaku, K., Tanaka, H., Tanaka, R., Tanaka, T., Togashi, T., Togawa, K., Tokuhisa, A., Tomizawa, H., Tono, K., Wu, S., Yabashi, M., Yamaga, M., Yamashita, A., Yanagida, K., Zhang, C., Shintake, T., Kitamura, H. & Kumagai, N. (2012). *Nat. Photon.* **6**, 540–544.
- Lafferty, J. M. (1951). *J. Appl. Phys.* **22**, 299–309.
- Lu, Z., Yin, S., Zhang, Z., Ren, F. & Lv, X. (2020). *Materials*, **13**, 100.
- Lu, Z., Zhang, Z., Yin, S. & Ren, F. (2018). *IEEE International Vacuum Electronics Conference (IVEC)*, 24–26 April 2018, Monterey, CA, USA, pp. 239–240. IEEE.
- Magnuson, M., Butorin, S. M., Guo, J.-H., Agui, A., Nordgren, J., Ogasawara, H., Kotani, A., Takahashi, T. & Kunii, S. (2001). *Phys. Rev. B*, **63**, 075101.
- Mitra, C., Hu, Z., Raychaudhuri, P., Wirth, S., Csiszar, S. I., Hsieh, H. H., Lin, H.-J., Chen, C. T. & Tjeng, L. H. (2003). *Phys. Rev. B*, **67**, 092404.
- Shirasawa, K., Tanaka, T., Seike, A., Hiraya, H., Kitamura (2004). *AIP Conf. Proc.*, **705**, 203–206.
- Tanaka, T., Nishitani, R., Oshima, C., Bannai, E. & Kawai, S. (1980). *J. Appl. Phys.* **51**, 3877–3883.
- Telieps, W. & Bauer, E. (1985). *Ultramicroscopy*, **17**, 57–65.
- Togawa, K., Shintake, T., Inagaki, T., Onoe, K., Tanaka, T., Baba, H. & Matsumoto, H. (2007). *Phys. Rev. ST Accel. Beams*, **10**, 020703.
- Woicik, J. C. (2016). Editors. *Hard X-ray Photoelectron Spectroscopy (HAXPES)*. Springer.
- Senba, Y., Ohashi, H., Kishimoto, H., Miura, T., Goto, S., Shin, S., Shintake, T. & Ishikawa, T. (2007). *AIP Conf. Proc.* **879**, 718–721.